

## Quantum Control of Photoelectron Circular Dichroism

R. Esteban Goetz,<sup>1</sup> Christiane P. Koch,<sup>2</sup> and Loren Greenman<sup>1,\*</sup>

<sup>1</sup>*Department of Physics, Kansas State University, 116 Cardwell Hall, 1228 North 17th Street, Manhattan, Kansas 66506-2601, USA*

<sup>2</sup>*Theoretische Physik, Universität Kassel, Heinrich-Plett-Strasse 40, D-34132 Kassel, Germany*



(Received 11 September 2018; published 10 January 2019)

We demonstrate coherent control over the photoelectron circular dichroism in randomly oriented chiral molecules, based on quantum interference between multiple photoionization pathways. To significantly enhance the chiral signature, we use a finite manifold of indistinguishable ( $1 + 1'$ ) resonantly enhanced multiphoton ionization pathways interfering at a common photoelectron energy but probing different intermediate states. We show that this coherent control mechanism maximizes the number of molecular states that constructively contribute to the dichroism at an optimal photoelectron energy and thus outperforms other schemes, including interference between opposite-parity pathways driven by bichromatic ( $\omega, 2\omega$ ) fields as well as sequential pump-probe ionization.

DOI: 10.1103/PhysRevLett.122.013204

Chiral molecules are nonsuperimposable mirror images of each other, referred to as enantiomers. Recent advances in measuring enantiomer-sensitive observables in gas phase tabletop experiments [1–4] have brought chiral molecules into the spotlight of current atomic, molecular and optical (AMO) research. One of these observables is photoelectron circular dichroism (PECD), i.e., the differential photoelectron angular distribution obtained by ionizing randomly oriented molecules with left-circularly and right-circularly polarized light [1,5–9]. PECD is a purely electric dipole effect, yielding much stronger signals than traditional absorption circular dichroism, which involves also the magnetic dipole of the probed transition. It can be quantified by the odd-moment coefficients in the expansion of the photoelectron angular distribution into Legendre polynomials. The simplest explanation for PECD is provided by perturbation theory for one-photon ionization [10]: It is the small difference in magnitude between dipole matrix elements with opposite sign  $m$  quantum number, occurring only for chiral molecules, that results in a net effect when averaging over all molecular orientations. More intuitively, two nonparallel vectors are needed to provide an orientation with which to probe the handedness of the molecular scaffold and create a pseudoscalar observable. While in traditional circular dichroism these are the electric and magnetic dipole moment, the photoelectron momentum provides the second vector in PECD. This picture connects PECD with the general framework for electric-dipole-based chiral observables [11]. Perturbation theory can also explain the PECD observed in resonantly enhanced multiphoton ionization (REMPI) [1], in terms of the electronically excited intermediate state of the REMPI process [12]. Dependence of the chiral signal on excitation wavelength is then understood in terms of probing different intermediate states [13]. Whether PECD is amenable to coherent

control by suitably shaping the ionizing pulses is an open question [14].

Here, we address this question by making use of optimal control theory and show that, for a chiral methane derivative, CHBrCIF, quantum interference between distinct two-photon ionization pathways significantly enhances PECD. To this end, we combine an optimization technique [18] with a many-body description of the electron dynamics, scattering theory to efficiently describe the photoelectron continuum [15–17], and second-order time-dependent perturbation theory with an optimization technique [18]. We use this approach to maximize the PECD for CHBrCIF while fully accounting for the chiral nature of the potential experienced by the photoelectron. We use CHBrCIF as one of the simplest chiral molecules that has featured prominently in recent experiments [3] but expect our findings to be relevant for larger molecules as well.

We first detail our methodology to calculate the photoelectron spectrum and PECD. Keeping the nuclei fixed and neglecting relativistic effects, the Schrödinger equation for the many electron system reads

$$i \frac{\partial}{\partial t} |\Psi^N(t)\rangle = [\hat{H}_0 + \hat{H}_1 - \mathcal{E}(t) \cdot \hat{\mathbf{r}}] |\Psi^N(t)\rangle, \quad (1)$$

where  $\hat{H}_0$  and  $\hat{H}_1$  refer to the mean-field Fock operator and the residual Coulomb interaction, respectively. Accounting for one-particle one-hole excitations only, the many-body wave function is described by the manifold [19]

$$|\Psi^N(t)\rangle = \alpha_0(t) e^{-ie_0 t} |\Phi_0\rangle + \sum_{i,a} \alpha_i^a(t) e^{-ie_i^a t} |\Phi_i^a\rangle + \sum_i \int d\mathbf{k} \alpha_i^k(t) e^{-ie_i^k t} |\Phi_i^k\rangle, \quad (2)$$

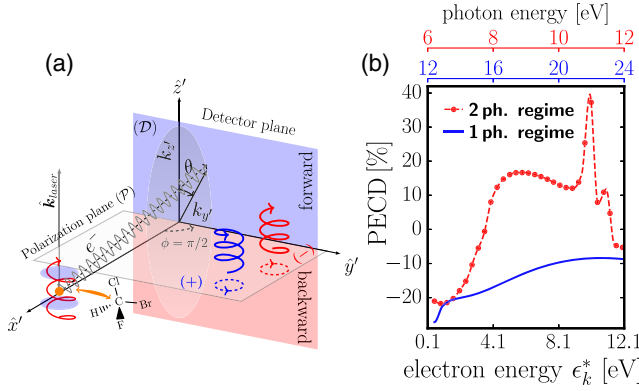


FIG. 1. (a) A randomly oriented ensemble of CHBrClF molecules (orange ball) is ionized with left-circularly (+) or right-circularly (−) polarized light, and the emitted electron is measured in the  $(z', y')$  plane. The polarization plane ( $\mathcal{P}$ ) defines the  $(x', y')$  plane and the vector  $z'$  normal to  $\mathcal{P}$  is given by the laser propagation direction. (b) Maximum PECD over all angles as a function of the photoelectron energy after ionization by a Gaussian pulse with central frequency  $\omega$  denoted in terms of photon energy. The photon order is determined using the anisotropy parameters in Eq. (8).

where  $\alpha_0(t)$ ,  $\alpha_i^a(t)$ , and  $\alpha_i^k(t)$  are time-dependent coefficients, and  $|\Phi_0\rangle$  refers to the Hartree-Fock ground state.  $|\Phi_i^a\rangle = \hat{c}_a^\dagger \hat{c}_i |\Phi_0\rangle$  and  $|\Phi_i^k\rangle$  describe one-particle one-hole excitations from an initially occupied orbital  $i$  to a bound unoccupied orbital  $a$  or a continuum state with energy  $|\mathbf{k}|^2/2$ . To model an ensemble of randomly oriented molecules, we average over all Euler angles  $\gamma_{\mathcal{R}} = (\alpha, \beta, \gamma)$ ; see Supplemental Material [20] for a detailed description. The orientation-averaged photoelectron momentum distribution is obtained upon integration over  $\gamma_{\mathcal{R}}$  and incoherent summation over the initially occupied contributing orbitals  $i$  in the Hartree-Fock ground state,

$$\frac{d^2\sigma}{d\epsilon_k d\Omega_{\mathbf{k}'}} = \sum_{i \in \text{occ}} \int |\alpha_i^k(t; \gamma_{\mathcal{R}})|^2 d^3\gamma_{\mathcal{R}}, \quad (3)$$

for  $t \rightarrow \infty$  and with  $\mathbf{k}'$  denoting the momentum measured in the laboratory frame, defined by the propagation direction of the light beam along  $z'$ , as indicated in Fig. 1(a). The photoionization process is captured by the coefficients  $\alpha_i^k(t; \gamma_{\mathcal{R}})$ . It requires an accurate description of the scattering portion of the wave function, which presents a formidable computational challenge for a many-electron system with no symmetry. To reduce the computational cost, we resort to solving Eq. (1) perturbatively. A second-order treatment allows us to manipulate quantum interferences between conventional opposite-parity, as well as same-parity (two-photon), pathways. These interferences can be exploited to control the differential and integral cross section in systems with no inversion center of

symmetry [28,29]. Restricting the maximum field amplitude and the ionization yield to ensure the validity of the perturbation approximation, Eq. (3) simplifies to

$$\frac{d^2\sigma}{d\epsilon_k d\Omega_{\mathbf{k}'}} \approx \int |\alpha_{i_0}^{k'(1)}(t; \gamma_{\mathcal{R}}) + \alpha_{i_0}^{k'(2)}(t; \gamma_{\mathcal{R}})|^2 d^3\gamma_{\mathcal{R}}, \quad (4)$$

for  $t \rightarrow \infty$  and with  $\alpha_{i_0}^{k'(1,2)}(t; \gamma_{\mathcal{R}})$ , the first-order (second-order) correction [20]. Second-order terms account for two-photon ionization pathways, from  $i_0$  to  $\mathbf{k}'$  via different unoccupied orbitals  $a$ .

We restrict the electron dynamics to be influenced by the mean-field molecular electrostatic potential and time-dependent field only. The orbitals participating during the photoionization are described by the manifold of the HOMO (labeled  $i_0$ , with ionization potential  $\omega_0$ ) and unoccupied orbitals defined by the eigenfunctions of the field-free Fock operator together with the scattering states defined by the excitation  $|\Phi_{i_0}^k\rangle$ . The Hartree-Fock orbitals were obtained using the MOLPRO [26,27] program package with the aug-cc-pVDZ basis set [30]. The scattering portion  $\varphi_{\mathbf{k}}^-(\mathbf{r})$  of the total wave function is an eigenfunction of the scattering problem,

$$\left(-\frac{\nabla^2}{2} - \frac{1}{r} + \hat{\mathbf{V}} - \frac{k^2}{2}\right)\varphi_{\mathbf{k}}^-(\mathbf{r}) = 0, \quad (5)$$

where  $\hat{\mathbf{V}}(\mathbf{r})$  is the short-range part of the electron-ion interaction. Equation (5) is solved using a locally modified version of the ePolyscat program package [15–17]; see the Supplemental Material [20] for more details. PECD is calculated by expanding Eq. (4) into Legendre polynomials  $P_\ell^m$ ,

$$\frac{d^2\sigma^{(\pm)}}{d\epsilon_k d\Omega_{\mathbf{k}'}} = \sum_{\ell, m} \beta_{\ell, m}^{(\pm)}(\epsilon_k) P_\ell^m(\cos\theta) e^{im\phi}, \quad (6)$$

where  $\pm$  distinguishes the momentum distribution obtained with left-circularly (+) and right-circularly (−) polarized light. The anisotropy parameters  $\beta_{\ell, m}^{(\pm)}(\epsilon_k)$  are decomposed into contributions from the one- and two-photon ionization pathways and their interference:

$$\beta_{\ell, m}^{(\pm)}(\epsilon_k) = \beta_{\ell, m}^{(\pm)1\text{ph}}(\epsilon_k) + \beta_{\ell, m}^{(\pm)2\text{ph}}(\epsilon_k) + \beta_{\ell, m}^{(\pm)\text{int}}(\epsilon_k). \quad (7)$$

PECD is the nonvanishing component that remains after subtracting Eq. (6) obtained with left- and right-circularly polarized light [1,5–9] and reads [20], for  $\phi = \pi/2$ ,

$$\begin{aligned} \text{PECD}(\epsilon_k, \theta, \phi = \pi/2) &= 2 \sum_{n, k} \beta_{2k+1, 0}^{(+)\text{mph}}(\epsilon_k) P_{2k+1}^0(\cos\theta) \\ &+ 6\text{Im}[\beta_{2, 1}^{(+)\text{int}}(\epsilon_k)] \sin(2\theta). \end{aligned} \quad (8)$$

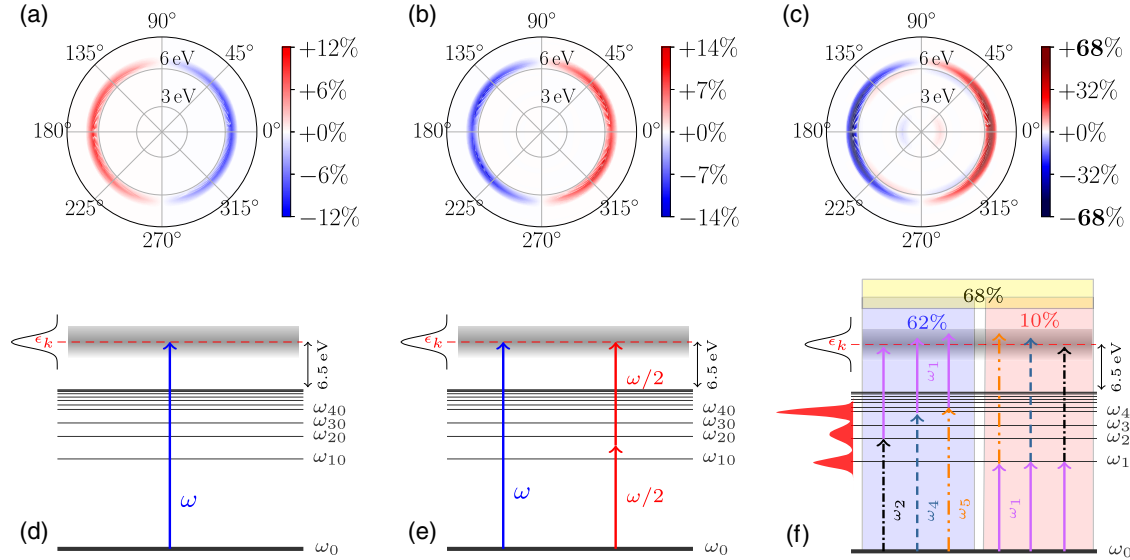


FIG. 2. (a)–(c) Angularly resolved PECD obtained with (a) a monochromatic reference field driving one-photon ionization, (b) an optimized bichromatic  $(\omega, 2\omega)$  pulse, and (c) making use of interference in even-parity two-photon pathways. (d)–(f) Corresponding ionization schemes. The control mechanism for two-photon pathway interference (f) is based on probing different intermediate states that interfere constructively at a common continuum photoelectron energy within the spectral bandwidth. Restricting the control mechanism to the pump-probe scenario with time-delayed pulses results in a maximum PECD of 62% (10%), whereas pulses overlapping in time realize the maximum PECD of 68%.

Anisotropy parameters and PECD are expressed in percentage of the peak photoelectron intensity. The driving electric field is parametrized,

$$\epsilon(t) = \sum_{j=1} \epsilon_j e^{-(t-\tau_j)^2/2\sigma_j^2} \cos[\omega_j(t-\tau_j) + \phi_j], \quad (9)$$

with  $\epsilon_j$ ,  $\omega_j$ ,  $\phi_j$  the amplitude, frequency, and carrier envelope phase of the  $j$ th pulse with full width at half maximum  $\text{FWHM} = 2\sqrt{2 \ln 2} \sigma_j$  and time delay  $\tau_j$ , which are optimized following Ref. [18]. To ensure the validity of the perturbation approximation, we constrain the maximal peak intensity to values not exceeding  $1.0 \times 10^{11} \text{ W/cm}^2$ , which was found to be an appropriate upper limit in bichromatic photoionization studies [31].

We first resolve the PECD as a function of the photon energy using a 25 fs (FWHM) monochromatic laser field [single frequency component in Eq. (9)] with peak intensity  $I_0 = 5 \times 10^{10} \text{ W/cm}^2$ . The resulting single- and two-photon PECD as a function of the photoelectron energy are shown in Fig. 1(b). Figure 2(a) shows the angularly resolved PECD for a photon energy of 18.4 eV. We now address the question of whether the PECD can be enhanced by allowing for more ionization pathways including their interference to contribute.

The use of quantum interference between one- and two-photoionization pathways is a general, well-documented control mechanism [28,29,31,32], and bichromatic pulses have been suggested to realize this scenario for atoms using

linearly [32] and circularly [31] polarized light. Control of anisotropy after bichromatic ionization is also predicted for randomly oriented chiral molecules [33]. In this Letter, we demonstrate, however, that interference between distinct two-photon ionization pathways results in a more efficient control mechanism to maximize PECD.

To this end, we first optimize driving fields constraining the frequency components to bichromatic  $(\omega, 2\omega)$  pulses. The PECD resulting from the optimized bichromatic  $(\omega, 2\omega)$  pulse reaches a maximum PECD of 20% at a photoelectron energy of 10 eV. This is comparable to asymmetries predicted for  $(\omega, 2\omega)$  bichromatic fields, linearly polarized in two mutually orthogonal directions employing rotationally tailored laser pulses for control [33]. In a second step, we allow complete freedom for the photon energies of the driving field. With a maximal peak intensity of  $3.5 \times 10^{10} \text{ W/cm}^2$  (for a total ionization yield of 6%), the fully optimized field is found to significantly enhance the PECD to 68%. The corresponding photoelectron spectrum peaks at an energy of 6.5 eV.

PECD is known to strongly depend on the final continuum states. It is therefore important to disentangle the kinetic energy effects, i.e., contributions arising from the final continuum state—here with energy 6.5 and 10 eV—and those from different photoionization pathways leading to the same final state. We therefore compare the PECD obtained with a reference field driving one-photon ionization, the optimized bichromatic  $(\omega, 2\omega)$ , and fully optimized pulses resulting in the same photoelectron kinetic energy.

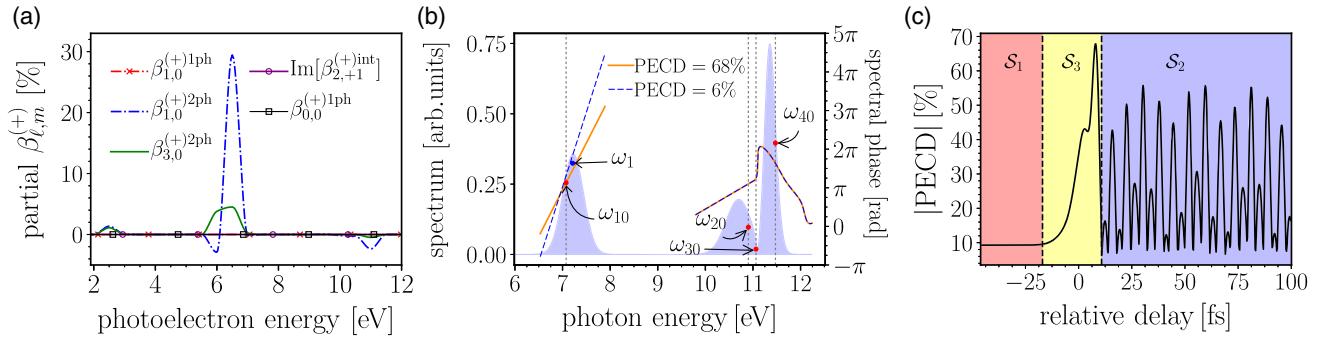


FIG. 3. (a) Anisotropy parameters for the fully optimized field as used in Fig. 2(c). (b) Spectrum (blue) and spectral phase (solid orange line) of the fully optimized pulse. The frequencies  $\omega_{j0}$  denote the transition energies between the HOMO and LUMO +  $j - 1$  orbitals. Modifying the spectral phase (orange solid versus blue dashed lines) while keeping the spectrum unchanged dramatically alters the PECD. (c) Maximum PECD as a function of the time delay between the  $\omega_1$  component and the higher-frequency components of the optimized pulse shown in (b). In regions  $\mathcal{S}_1$  and  $\mathcal{S}_2$ , the subpulses are temporally separated (pump-probe scenario) with  $\mathcal{S}_1$  corresponding to ionization via the LUMO only [cf. right-hand part of Fig. 2(f)], whereas in  $\mathcal{S}_2$ , ionization proceeds via a superposition of different excited states without the LUMO [cf. left-hand part of Fig. 2(f)]. In  $\mathcal{S}_3$ , pump and probe pulses overlap in time such that interference between all two-photon ionization pathways can be exploited.

The results for a photoelectron kinetic energy of 6.5 eV are shown in Fig. 2, whereas those for 10 eV are found in the Supplemental Material [20]. At a photoelectron energy of 6.5 eV, the PECD is enhanced from 12% using one-photon ionization to 14% using an interfering two-photon ionization pathway, i.e., bichromatic control, whereas a single two-photon ionization pathway that does not include interference reaches 16.2% PECD at 6.5 eV, as shown in Fig. 1(b).

All of these are significantly smaller than 68% obtained for the fully optimized pulse where only two-photon pathways, but many more of them, cf. Fig. 2(f), interfere. This picture holds also at a photoelectron kinetic energy of 10 eV, where the maximum PECD for the reference field, optimized bichromatic ( $\omega$ ,  $2\omega$ ), and fully optimized pulses amounts to 8.5%, 20%, and 64%, respectively [20].

The control mechanism for the fully optimized field of Fig. 2(f) is further analyzed in Fig. 3, with Fig. 3(a) showing the different anisotropy parameters for the fully optimized pulse. In contrast to the reference and optimized bichromatic ( $\omega$ ,  $2\omega$ ) pulses, neither single-photon ionization nor interference between one- and two-photon pathways contributes for the fully optimized pulse. In fact, both  $\beta_{1,0}^{(+)\text{1ph}}$  and  $\beta_{2,+1}^{(+)\text{int}}$  vanish over the entire energy domain. Furthermore, the one-photon ionization pathway is completely suppressed, even for the symmetric part, since  $\beta_{0,0}^{(+)\text{1ph}} = 0$ . Instead, the remarkable enhancement of the PECD is indeed solely due to even-parity, i.e., two-photon ionization, pathways because both  $\beta_{1,0}^{(+)\text{2ph}}$  and  $\beta_{3,0}^{(+)\text{2ph}}$  are nonzero.

Analyzing the spectrum of the fully optimized field, shown in Fig. 3(b), we identify the interference between different two-photon ionization pathways to give rise to the control observed in Fig. 2(c). The spectrum contains peaks at

$\omega_1 = 7.24$  eV,  $\omega_2 = 10.70$  eV, and  $\omega_3 = 11.35$  eV and overlaps with transitions from the HOMO to the first unoccupied orbitals, namely,  $\omega_{10} = 7.07$  eV,  $\omega_{20} = 10.90$  eV,  $\omega_{30} = 11.06$  eV, and  $\omega_{40} = 11.47$  eV, which need to be compared to the calculated ionization threshold of 11.88 eV. The two-photon ionization pathway  $2 \times \omega_{10}$  promotes the photoelectron to 2.27 eV and explains the small peak at 2.39 eV in Fig. 3(a). Conversely, the pathways  $2 \times \omega_2$ ,  $\omega_2 + \omega_3$ ,  $\omega_2 + \omega_4$ , ... explain the small PECD at 11 eV. However, these pathways do not contribute much to PECD, which is mainly due to the peak at 6.5 eV. The most important pathways leading to 6.5 eV, cf. Fig. 2(f), are  $\omega_{20} + (\omega_{10} + \delta\omega_1)$  and similarly  $(\omega_{10} + \delta\omega_1) + \omega_{20}$  with an offset of  $\delta\omega_1 = 0.4$  eV as well as  $\omega_{40} + (\omega_{10} - \delta\omega)$  with  $\delta\omega = 0.12$  eV. The latter probes the LUMO + 3, whereas the former two probe the LUMO + 1 and LUMO. The required offsets are available within the spectral bandwidth. The pathways  $\omega_{30} + \omega_{10}$  and  $\omega_{10} + \omega_{30}$ , probing the LUMO + 2, are also compatible with the pulse spectrum; however, the frequency  $\omega_{30}$  is suppressed, and removing the LUMO + 2 decreases the PECD by only 0.4%. In other words, the high-frequency components of the optimized field correspond to photon energies which resonantly excite the first LUMO +  $j$  orbitals ( $j = 1, 2, \dots$ ), while the peak centered at  $\omega_1$  can either excite the LUMO from the ground state or ionize the LUMO +  $j$  population, cf. Fig. 2(f). Its bandwidth guarantees interference at a common photoelectron energy. Thus, the width and peak position at  $\omega_1$  are key for the constructive interference among a finite manifold of two-photon ionization pathways at a common final photoelectron energy to significantly enhance PECD. Constraining  $\omega_1$  to be exactly  $\omega_{10}$  while reducing its spectral bandwidth results in a smaller PECD ( $\approx 50\%$ ). Conversely, allowing  $\omega_1$  to be further blueshifted with respect to  $\omega_{10}$  while increasing

the spectral bandwidth such that it still overlaps with  $\omega_{10}$  results in a PECD of about 70% (not shown due to the large bandwidth of the field).

The coherent nature of the control mechanism is further confirmed by modifying the spectral phase of the optimized pulse while keeping the spectral amplitude unaffected, cf. dashed lines in Fig. 3(b). This corresponds to introducing a time delay between the high- and low-frequency components of the pulse. Figure 3(c) shows the variation of the PECD, between 68% to 6%, as a function of this time delay. Positive (negative) delays correspond to the high-frequency components arriving before (after) the low-frequency components, as verified by inspecting the Wigner distribution function of the pulses. For negative time delays, highlighted in red in Figs. 2(f) and 3(c), only the LUMO is excited. PECD thus does not depend on the time delay and reflects the chiral signature of the LUMO only, which amounts to about 10%. For positive time delays, highlighted in blue in Figs. 2(f) and 3(c), the high-frequency components of the pulse prepare a superposition of higher excited states, such that the PECD depends on the time delay and contains the chiral fingerprints of the LUMO +  $j$  ( $j \geq 1$ ) with a maximum of 55%. These two scenarios correspond to pump-probe control [34,35], where the pump pulse spectrum selects the manifold of intermediate states that contribute. PECD can be pushed to 62% by further optimization of time-separated pump and probe pulses for positive delays. However, the maximal value of PECD, 68%, is obtained when pump and probe overlap, as highlighted in yellow in Figs. 2(f) and 3(c). This can be rationalized by exploiting interference of all the pathways, including the two-photon ionization through the LUMO, depicted in Fig. 2(f).

In conclusion, we have identified constructive interference in two-photon photoionization to significantly enhance PECD of randomly oriented CHBrClF molecules. Control is achieved via various ( $1 + 1'$ ) REMPI pathways leading to a common final photoelectron state but probing different intermediate states. Separating pump and probe photons in time slightly reduces the number of pathways that may interfere and thus the PECD. In this excitation scheme based on interference of same-parity pathways, we find significantly larger PECD than can be obtained with optimized bichromatic circularly polarized fields where opposite parity pathways are made to interfere constructively. It will be straightforward to extend this type of control to molecules other than CHBrClF, with only the central frequencies and spectral widths depending on the specific chiral molecule. Higher-order terms in the perturbation expansion, while requiring larger amplitudes, are likely to facilitate even more pathway interference and could also be used to drive photoionization with optical instead of extreme ultraviolet pulses. Whether an upper bound to PECD exists and what type of driving field would saturate it is yet unknown.

We would like to thank Thomas Baumert for helpful comments on the manuscript. The computing for this project was performed on the Beocat Research Cluster at Kansas State University, which is funded in part by NSF Grants No. CNS-1006860, No. EPS-1006860, and No. EPS-0919443. C. P. K. acknowledges financial support from the Deutsche Forschungsgemeinschaft (CRC 1319).

\*lgreenman@phys.ksu.edu

- [1] C. Lux, M. Wollenhaupt, T. Bolze, Q. Liang, J. Köhler, C. Sarpe, and T. Baumert, *Angew. Chem., Int. Ed.* **51**, 5001 (2012).
- [2] D. Patterson, M. Schnell, and J. M. Doyle, *Nature (London)* **497**, 475 (2013).
- [3] M. Pitzer, M. Kunitski, A. S. Johnson, T. Jahnke, H. Sann, F. Sturm, L. P. H. Schmidt, H. Schmidt-Böcking, R. Dörner, J. Stohner, J. Kiedrowski, M. Reggelin, S. Marquardt, A. Schießler, R. Berger, and M. S. Schöffler, *Science* **341**, 1096 (2013).
- [4] P. Herwig, K. Zawatzky, M. Grieser, O. Heber, B. Jordon-Thaden, C. Krantz, O. Novotný, R. Repnow, V. Schurig, D. Schwalm, Z. Vager, A. Wolf, O. Trapp, and H. Kreckel, *Science* **342**, 1084 (2013).
- [5] N. Böwering, T. Lischke, B. Schmidtke, N. Müller, T. Khalil, and U. Heinzmann, *Phys. Rev. Lett.* **86**, 1187 (2001).
- [6] U. J. Meierhenrich, J.-J. Filippi, C. Meinert, J. H. Bredehöft, J.-i. Takahashi, L. Nahon, N. C. Jones, and S. V. Hoffmann, *Angew. Chem., Int. Ed.* **49**, 7799 (2010).
- [7] C. S. Lehmann, N. B. Ram, I. Powis, and M. H. M. Janssen, *J. Chem. Phys.* **139**, 234307 (2013).
- [8] A. Comby, S. Beaulieu, M. Boggio-Pasqua, D. Descamps, F. Légaré, L. Nahon, S. Petit, B. Pons, B. Fabre, Y. Mairesse, and V. Blanchet, *J. Phys. Chem. Lett.* **7**, 4514 (2016).
- [9] S. Beaulieu, A. Comby, A. Clergerie, J. Caillat, D. Descamps, N. Dudovich, B. Fabre, R. Géneaux, F. Légaré, S. Petit, B. Pons, G. Porat, T. Ruchon, R. Taïeb, V. Blanchet, and Y. Mairesse, *Science* **358**, 1288 (2017).
- [10] B. Ritchie, *Phys. Rev. A* **13**, 1411 (1976).
- [11] A. F. Ordonez and O. Smirnova, *Phys. Rev. A* **98**, 063428 (2018).
- [12] R. E. Goetz, T. A. Isaev, B. Nikoobakht, R. Berger, and C. P. Koch, *J. Chem. Phys.* **146**, 024306 (2017).
- [13] A. Kastner, T. Ring, B. C. Krüger, G. B. Park, T. Schäfer, A. Senftleben, and T. Baumert, *J. Chem. Phys.* **147**, 013926 (2017).
- [14] M. Wollenhaupt, *New J. Phys.* **18**, 121001 (2016).
- [15] F. A. Gianturco, R. R. Lucchese, and N. Sanna, *J. Chem. Phys.* **100**, 6464 (1994).
- [16] A. P. P. Natalense and R. R. Lucchese, *J. Chem. Phys.* **111**, 5344 (1999).
- [17] L. Greenman, R. R. Lucchese, and C. W. McCurdy, *Phys. Rev. A* **96**, 052706 (2017).
- [18] R. E. Goetz, M. Merkel, A. Karamatskou, R. Santra, and C. P. Koch, *Phys. Rev. A* **94**, 023420 (2016).
- [19] T. Klamroth, *Phys. Rev. B* **68**, 245421 (2003).
- [20] See Supplemental Material at <http://link.aps.org/supplemental/10.1103/PhysRevLett.122.013204> for a detailed description of our methods as well as photoelectron

- angular distributions at a final kinetic energy of 10 eV. Supplemental Material also contains Refs. [15–18,21–27].
- [21] A. Szabo and N. S. Ostlund, *Modern Quantum Chemistry: Introduction to Advanced Electronic Structure Theory* (Dover Publications, 1996).
- [22] M. Baertschy, T. N. Rescigno, and C. W. McCurdy, *Phys. Rev. A* **64**, 022709 (2001).
- [23] W. H. Miller and B. M. D. D. Jansen op de Haar, *J. Chem. Phys.* **86**, 6213 (1987).
- [24] N. Rohringer, A. Gordon, and R. Santra, *Phys. Rev. A* **74**, 043420 (2006).
- [25] A. R. Edmonds, *Angular Momentum in Quantum Mechanics* (Princeton University Press, Princeton, 2016).
- [26] H.-J. Werner *et al.*, <http://www.molpro.net>.
- [27] H.-J. Werner, P. J. Knowles, G. Knizia, F. R. Manby, and M. Schtz, *WIREs Comput. Mol. Sci.* **2**, 242 (2012).
- [28] M. Shapiro and P. Brumer, *Rep. Prog. Phys.* **66**, 859 (2003).
- [29] M. Shapiro and P. Brumer, *Quantum Control of Molecular Processes* (Wiley-VCH, Weinheim, 2012), p. 561.
- [30] R. A. Kendall, T. H. Dunning, Jr., and R. J. Harrison, *J. Chem. Phys.* **96**, 6796 (1992).
- [31] N. Douguet, A. N. Grum-Grzhimailo, E. V. Gryzlova, E. I. Staroselskaya, J. Venzke, and K. Bartschat, *Phys. Rev. A* **93**, 033402 (2016).
- [32] N. Douguet, A. N. Grum-Grzhimailo, and K. Bartschat, *Phys. Rev. A* **95**, 013407 (2017).
- [33] P. V. Demekhin, A. N. Artemyev, A. Kastner, and T. Baumert, *Phys. Rev. Lett.* **121**, 253201 (2018).
- [34] D. Tannor and S. Rice, *J. Chem. Phys.* **83**, 5013 (1985).
- [35] D. J. Tannor, R. Kosloff, and S. A. Rice, *J. Chem. Phys.* **85**, 5805 (1986).